FULL PAPER

Donor-Induced Performance Tuning of Amorphous SrTiO₃ Memristive Nanodevices: Multistate Resistive Switching and Mechanical Tunability

Hussein Nili,* Sumeet Walia, Ahmad Esmaielzadeh Kandjani, Rajesh Ramanathan, Philipp Gutruf, Taimur Ahmed, Sivacarendran Balendhran, Vipul Bansal, Dmitri B. Strukov, Omid Kavehei, Madhu Bhaskaran, and Sharath Sriram*

Metal–oxide valence-change memristive devices are the key contenders for the development of multilevel nonvolatile analog memories and neuromorphic computing architectures. Reliable low energy performance and tunability of nonlinear resistive switching dynamics are essential to streamline the high-density circuit level integration of these devices. Here, manipulation of room temperature-synthesized defect chemistry is employed to enhance and tune the switching characteristics of high-performance amorphous SrTiO₃ (*a*-STO) memristors. Substitutional donor (Nb) doping with low concentrations in the *a*-STO oxide structure allows extensive improvements in energy requirements, stability, and controllability of the memristive performance, as well as field-dependent multistate resistive switching. Evidence is presented that room temperature donor doping results in a modified insulator oxide where dislocation sites act as charge carrier modulators for low energy and multilevel operation. Finally, the performance of donor-doped *a*-STO-based memristive nanodevices is showcased, with the possibility of mechanical modulation of the nonlinear memristive characteristics of these devices demonstrated. These results highlight the potential of donor-doped *a*-STO nanodevices for high-density integration as analog memories and multifunctional alternative logic elements.

1. Introduction

Highly nonlinear and nonvolatile memristive characteristics of two-terminal capacitor-like metal-insulator-metal (MIM) devices based on transition metal oxides have attracted intensified research interest[1–5] due to their potential for the development of highly scalable memory devices. They also promise to be the precursors for novel computer architectures and unconventional computing such as neuromorphic engineering.[2,3,6]

Among transition metal oxides, the prototypical perovskite strontium titanate SrTiO₃ (STO) system has emerged

as a promising candidate for the functional oxide layer in memristive MIM devices.[2,7–10] Its self-doping tendency with oxygen vacancies subject to electrical or thermal stress can transform its electronic structure from a band insulator to a metallic conductor and facilitate electroresistive switching suitable for two-terminal memory devices.[11,12] The resistive switching in STO-based devices is generally attributed to highly localized accumulation of oxygen vacancies (i.e., nanofilaments) along the extended defect structures, which result in the local bypassing of the depletion layer at the metal–oxide interfaces.[2,6,8,11,13–16] Additionally, the defect structure of STO can be directly manipulated via doping with a donor- or acceptor-type transition metal, which can be employed to modulate the electronic structure at local (e.g., grain boundaries and point defects) and bulk levels.[10,14,17–19] This can be used as a tool to engineer the arrangement and electronic/ionic transport properties of nanofilaments, and therefore, the memristive properties of STO-based devices.[13,14] As such, STO-based devices have the potential for high-density integration as passive memory elements in digital systems operating in ultra-high-frequency regimes.[3,14] Moreover, the tunability of STO structure with respect to coupled electromechanical and electro-optical effects highlights the impressive degree of freedom it can render in the design of multifunctional nonlinear devices.[20–24]

Recently, we reported the realization of high-performance memristive MIM devices based on oxygen-deficient amorphous

Dr. H. Nili, Dr. S. Walia, P. Gutruf, T. Ahmed,
Dr. S. Balendhran, Dr. O. Kavehei,
Dr. M. Bhaskaran, Dr. S. Sriram
Functional Materials and Microsystems
Research Group and Micro Nano Research Facility
RMIT University
Melbourne, Victoria, Australia
E-mail: hussein.nili@gmail.com; sharath.sriram@rmit.edu.au

Dr. A. E. Kandjani, Dr. R. Ramanathan, Prof. V. Bansal
NanoBiotechnology Research Laboratory
School of Applied Sciences
RMIT University
Melbourne, Victoria, Australia

Prof. D. B. Strukov
Electrical and Computer Engineering Department
University of California Santa Barbara
Santa Barbara, CA, USA

www.MaterialsViews.com

ADVANCED
FUNCTIONAL
MATERIALS
www.afm-journal.de

FULL PAPER

SrTiO₃ (a-STO) oxides in a Pt/Ti/a-STO/Pt structure.[16] The as-grown oxygen vacancy point defect structure is found to facilitate the creation of a distributed nanofilament (nanoswitch) network across the device, which is responsible for the stable bipolar switching with high switching ratios and area-independent high- and low-resistance states (HRS and LRS). We also presented evidence of the impact of mechanical stress on the modulation of ionic transport in a-STO oxides though force-controlled nanocontact experiments.

Here, we investigate the defect chemistry of a-STO oxides in detail and its impact on the memristive performance of a-STO-based devices. Temperature stability, retention, and endurance of the devices have been analyzed through temperature-dependent electrical characterizations and their relations to the defect chemistry have been investigated. An experimental approach introduced recently by Messerschmitt et al.[25] has been applied for the electrical characterization of memristive kinetics in a-STO MIM devices. In particular, we report the effects of doping oxygen-deficient a-STO with niobium (Nb) donor species, which improves the overall switching performance and allows for multiple stable switching states in MIM devices. Moreover, force-controlled conductive nanocontact studies are utilized to study the switching dynamics of nanoswitches in MIM cells. Finally, we show the realization of individual Nb:a-STO nanoswitches in form of patterned nanoislands with 10 nm thickness and 300 nm diameter and report on the potential for mechanical modulation of their transport properties. These results make the case for ultimate high-density integration and immense multifunctionality potential of a-STO-based resistive memory devices.

2. Performance Tuning of a-STO MIM Cells

a-STO thin films were synthesized through RF magnetron sputtering at room temperature as the functional oxide layer for memristive devices (see Section S1, Supporting Information). Electrical and resistive switching properties of a-STO thin films with different compositions were investigated in a micron-sized cross-bar array configuration as illustrated in **Figure 1**a (see Methods for fabrication details). To investigate control over and ability to tune the performance of a-STO memristors, three film types were prepared for comparison: stoichiometric a-STO, oxygen-deficient a-STO, and Nb-doped oxygen-deficient a-STO.

As previously reported, the dissimilar metal–oxide interfaces facilitate robust redox processes and the subsequent creation of nanofilamentary extended defect structures during the electroforming process.[16] Particularly, a-STO forms an Ohmic interface with shallow work function (4.3 eV) Ti, which acts as the cathode (transparent to the ionic current) for redox reactions in the oxide layer.[2,26] Even prior to the creation of the extended defect structures, the Ti is partially oxidized at the vicinity of the interface with a-STO according to the reaction Ti + SrTiO₃ → TiOₓ + SrTiO₃₋ₓ.[26] The top Pt layer prevents further oxidization of the Ti layer, which can occur due to exposure to ambient oxygen.

All a-STO MIM devices were highly insulating in their virgin state and showed Schottky-like transport characteristics when biased from the bottom Pt electrode. Temperature dependence of virgin state conductivity of the a-STO MIM cells was measured in the 200–525 °C range under a voltage bias of 100 mV. In the case of stoichiometric a-STO, the activation energy for the majority electronic carriers in virgin state (i.e., the capacitive leakage current) was calculated to be 1.48 ± 0.03 eV using the slope of the Arrhenius plots of electrical conductivity (Figure 1b). This is in good agreement with the previously reported values for the activation energy of electronic carrier conduction in pristine STO.[25,27] For oxygen-deficient a-STO, the activation energy reduces to 1.39 eV, which can be explained by the higher concentration of as-grown vacancy related defect structures that result in more pronounced electronic conduction.[13,29] The calculated activation energy for Nb-doped oxygen-deficient a-STO is similar to the oxygen-deficient a-STO within an error margin of ±0.03 eV, which indicates that the Nb-induced dislocations are frozen as isolated sites in the virgin state and their thermal activation does not significantly impact the overall electronic transport owing to their extremely low concentration (Nb/Ti ratio of 0.02).

In order to achieve bipolar resistive switching, an electroforming procedure is typically required for STO-based MIM devices.[2,10,13,30,31] A single electroforming voltage sweep from the bottom Pt/a-STO interface (forming anode) was necessary to induce resistive switching behavior in our a-STO devices. A current compliance limit of 100 μA was set to prevent dielectric breakdown. Figure 1c shows the representative electroforming sweeps for devices utilizing a-STO thin films with different compositions. a-STO thin films with stoichiometric content are electroformed though voltage sweeps in the range of 11–13 V. Following the electroforming, the a-STO devices show bipolar switching characteristics under DC voltage sweeps with a sweep rate of 1 kHz (V_{SET} = <–1.1 V ± 25%>, V_{RESET} = <2.6 V± 22%>) with switching ratios within the range of 50–70 at a READ voltage of ±100 mV (Figure 1d). On the other hand, oxygen-deficient a-STO thin films require a peak voltage sweep range of 8–10 V during the electroforming step. The bipolar switching behavior of oxygen-deficient a-STO thin films is more stable and the switching ratios are significantly enhanced to 10^3–10^4 (V_{SET} = <–1.5 V ± 16%>, V_{RESET} = <2.9 V ± 18%>) at similar READ voltages. For Nb-doped oxygen-deficient a-STO thin films, required peak sweep voltages for electroforming drops significantly (5–6 V). The electroformed devices retain high switching ratios of ≈10^3 while showing reduced requirements for WRITE/ERASE and READ current densities (V_{SET} = <–1.1 V ± 14%>, V_{RESET} = <2.4 V ± 11%>) in both LRS and HRS, respectively, compared to other devices. Differences between the performance characteristics of different oxides are investigated and explained in detail in the following sections. More than 25 devices of each oxide composition with electrode sizes ranging from 20 × 20 to 100 × 100 μm² were tested using cyclic voltammetry. Long bias READ (100 mV for 10^5 s) at three different temperatures (27 °C, 85 °C, and 125 °C) and pulsed WRITE/READ/ERASE cycles (10^6 cycles, pulse widths of 10 μs) were used to confirm the endurance, stability, and uniformity of the a-STO devices (see Section S2, Supporting Information). The range was chosen to generate reproducible results before the onset of temperature degradation in MIM cells. Nb-doped oxygen-deficient oxides exhibited improvements in current density uniformity over multiple pulse cycles and overall state
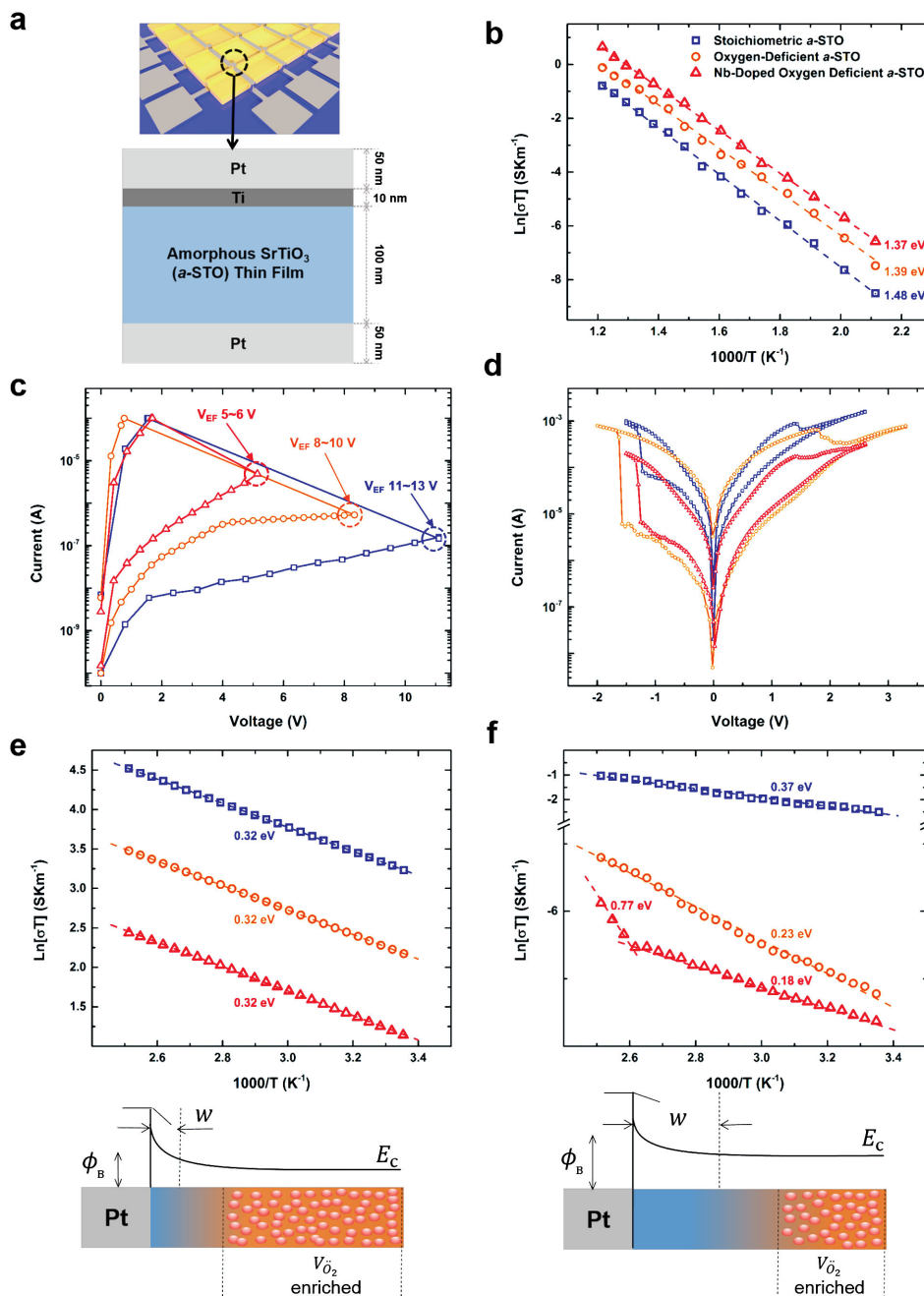
**ADVANCED
FUNCTIONAL
MATERIALS**

www.afm-journal.de

FULL PAPER

*Materials
Views*

www.MaterialsViews.com

Figure 1. a) Plan view and cross-sectional schematics of *a*-STO cross bar MIM structures, where three types of *a*-STO were investigated. b) Arrhenius-type plots for virgin state conduction activation energy under a 100 mV bias. c) Typical electroforming sweeps. d) Representative bipolar switching behavior averaged over repeated 10^4 voltammetry cycles for *a*-STO MIM cells utilizing different oxide layers. e) Low- and f) high-resistance state Arrhenius-type plot of conduction activation energies under a 100 mV bias. Schematics represent the perceived conduction mechanisms.

retention at ambient as well as elevated temperatures. This is largely due to reduced forming fields, which in turn result in less drastic dielectric degradation of the MIM cells; thereby, causing the suppression of parasitic leakage paths.

Figure 1e,f show the Arrhenius plots of the evolution of electrical conductivity in the LRS and HRS states for different oxides under a 100 mV bias, respectively. The conduction activation energies in the LRS regime are found to be similar for

all oxides. At such temperature range, READ bias is unlikely to activate ionic drift in the vicinity of the switching interface, even though mixed electronic/ionic transport mechanisms are responsible for LRS conduction in the bulk of oxide. Therefore, LRS activation energies likely pertain to electrons tunneling through the reduced residual barrier at Pt/*a*-STO interface.[32,33] This indicates that the formed filamentary pathways have similar electronic and defect structures in the

www.MaterialsViews.com

ADVANCED
FUNCTIONAL
MATERIALS
www.afm-journal.de

FULL PAPER

different stoichiometries of STO used in this study. The differences in the conductivity of different oxides can be justifiably explained by the variations in overall degradation of the oxide layers[11] and thinning of the depletion layer at the bottom Pt/a-STO interface[11,12,31] subject to increasing forming fields. On the other hand, in the HRS regime, electrical conduction is governed by the partially recovered Schottky barrier at this Pt/a-STO interface and the current transport likely originates from the contribution of majority electronic carriers (leakage) at the recovered residual barrier.[16,31] The reduction in the HRS activation energy of oxygen-deficient a-STO compared to stoichiometric a-STO verifies the impact of vacancy dislocation sites in facilitating the electronic/ionic transport in the HRS regime. The activation energy of Nb-doped oxygen-deficient oxide is further lowered at the lower end of the temperature range, where the leakage current contribution at the active interface is dominant, presumably due to the high concentration of n-type electronic carriers.[34] At the higher end of the temperature range, an apparent transition temperature is observed. This can be tentatively ascribed to the thermal activation of ionic diffusion at the donor dislocation sites. Donor dislocation sites in STO structure act as carrier trap sites in the oxide layer, possibly due to selective oxidation.[35] The ionic diffusion of oxygen species at these sites has a relatively higher activation energy than the rest of electroformed oxide. However, a more thorough analysis is required to underpin the exact nature of biphasic conduction's temperature dependence in Nb-doped MIM cells.

These results depict a consistent picture of the impact of as-grown vacancy-related defect structures and donor dislocation sites on the tuning of memristive performance in a-STO MIM devices. The positively charged oxygen vacancies accumulated in the virtual cathode region act as donor-type (n-conducting) centers in the a-STO lattice; thereby, increasing the overall electronic conductivity.[2,9] Moreover, vacancy-induced point and line defects act as fast transport routes for ionic transport and provide a guiding network for the creation of extended defects.[9,15,36] As the oxygen exchange reactions in STO take place at oxygen vacancy dislocation sites, ordered vacancies along such line defects exhibit an ionic conductivity, which is several orders of magnitude higher than the insulating bulk oxide. Therefore, an increase in vacancy concentration in oxygen-deficient a-STO reduces the electrical stress required for the creation of extended defect structures, which results in lower dielectric degradation during the forming process. The introduction of donor Nb further increases the overall electronic conductivity (through introduction of n-type electronic carriers).[34,35,37] It is well known that grain boundaries in donor-doped STO crystal are highly resistive due to selective oxidation of the bulk phase in their vicinity.[34,35] In the oxygen-deficient amorphous oxide, donor-induced dislocation sites add an additional guiding vector for the ionic transport and creation of extended vacancy defect structures. Further, carrier trap sites can be generated at the Nb donor centers during the forming process[17] with a higher conduction activation energy than the rest of the formed oxide, which can be exploited for further tuning of the memristive performance. The existence of the carrier trap sites at the vicinity of the switching interface is hypothesized based on the biphasic conduction activation

energy in HRS regime and further material and electrical characterizations discussed later in the this report.

To substantiate this hypothesis, a long bias experiment was carried out following a similar methodology described by Messerschmitt et al.[25] as follows: active MIM cells with different oxide layers were switched between LRS and HRS under constant voltage biases ranging from 65% to 95% of the RESET voltage, and 95% of the SET voltage, respectively. This was done by keeping a constant bias on the device for an hour. HRS currents were monitored for 10^4 s under a 100 mV READ voltage after each long bias step to verify the state transition and retention. The devices were set back to LRS after every individual RESET step via constant biasing at their designated SET voltage for one hour, to ensure that the devices are back to their steady equilibrated LRS before carrying out the subsequent RESET step.

Although during the OFF operation in all three oxide systems, multiple intermediate states are accessible (Figure 1d), in stoichiometric and oxygen-deficient a-STO cells these states ultimately stabilize to the most stable high-resistance state (i.e., complete OFF) subject to sustained DC biases (one hour duration) greater that 65% of the average RESET voltage. As such, these field-dependent intermediate states are transient in nature, and chiefly rely on the transient distribution of oxygen vacancies through the conductive filament(s). In contrast, Nb-doped oxygen-deficient oxide shows multiple discernible and stable high-resistance states, as demonstrated in **Figure 2**a,b. This further points to the existence of electronic/ionic charge trap or intermediate valence band energy states within the formed donor-doped oxide layer. Pulse WRITE/READ/ERASE experiments with variable RESET voltages on Nb-doped oxide cells further demonstrate accessibility and stability of these additional states in the normal memristive operation of MIM cells. Subject to constant SET and variable RESET voltages (Figure 2c), the cells switch between a single low-resistance and multiple discernible high-resistance states (Figure 2d,e). Figure 2f demonstrates the endurance of the distinct resistance states over 10^5 switching cycles. Cell resistance in the LRS retains a relatively low margin of deviation (average standard deviation of 17.4% over a full cycle and 7.1% between cycles over 10^5 cycles). On the other hand, the six high-resistance states, with a minimum resistance separation of 15.1% (between HRS_4 and HRS_5) are consistently distinct over 10^5 switching cycles. Thus, the doping of oxygen-deficient a-STO with donor Nb sites allows for the fine tuning of memristive performance and the realization of stable and reliable multistate logic elements.

3. Defect Chemistry of a-STO MIM Cells

It is well known that the defect structure in the transition metal oxides resulting from intermediate chemical phases and oxygen vacancy induced point and line defects, largely determine the memristive behavior of metal oxide-based MIM devices.[1–4,13,15,30,32,38] In order to investigate the chemical states in a-STO thin films and the impact of the compositional changes on the memristive behavior of a-STO MIM devices, a detailed analysis of the X-ray photoelectron spectroscopy (XPS)-binding
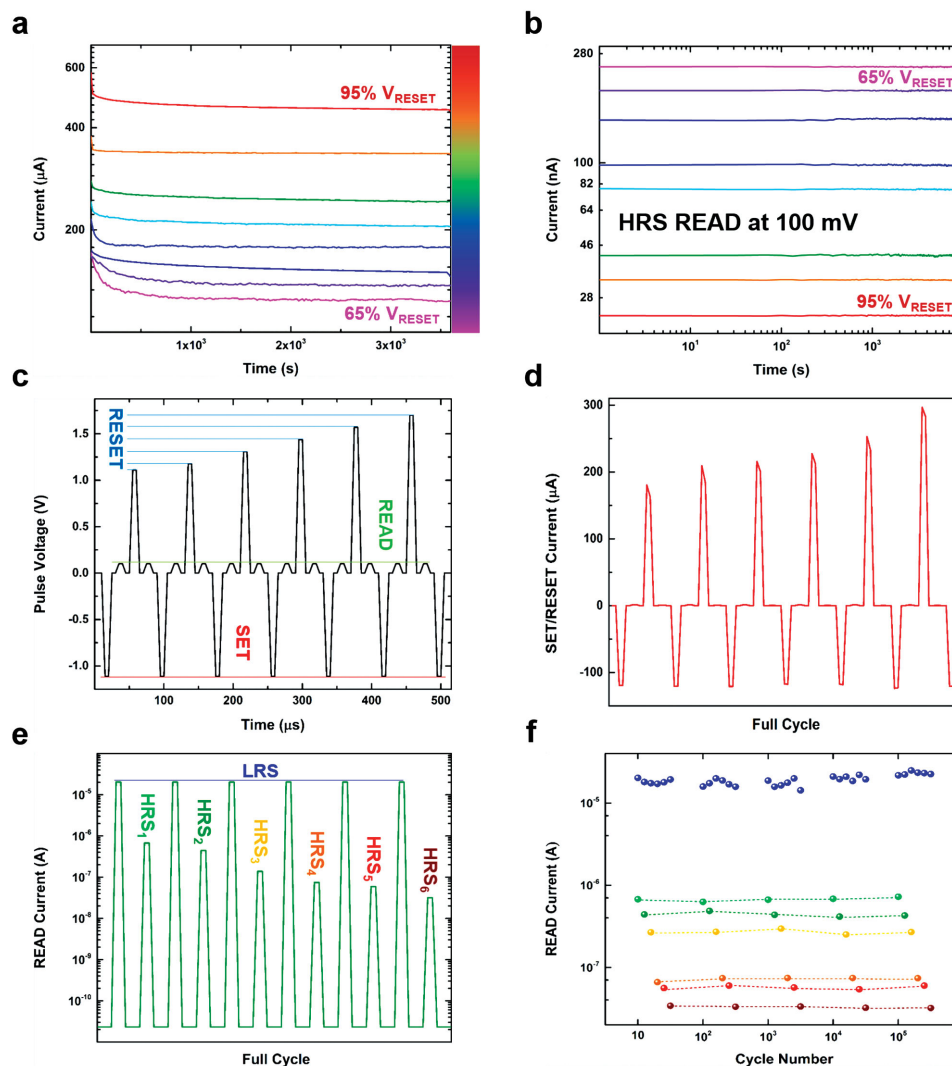
ADVANCED
FUNCTIONAL
MATERIALS
www.afm-journal.de

Materials
Views
www.MaterialsViews.com

FULL PAPER

Figure 2. Long bias and complementary multistate pulse experiments on Nb-doped a-STO MIM cells. a) Current evolution of MIM cells in LRS subject to application of progressive constant RESET voltages over one hour. b) Current retention over 10^4 s after each long bias RESET step under a 100 mV READ voltage. c) A full SET/READ/RESET pulse cycle with constant SET (-1.1 V) and READ (100 mV) and increasing RESET (1.1–1.7 V) voltages. All pulses have a duration of 10 µs. d) Representative SET/RESET current response and e) READ currents of the MIM cell over one full SET/READ/RESET cycle. f) Endurance of single LRS and multiple HRS states over 10^5 full switching cycles (power of 10 cycle numbers are depicted).

energy spectra of the principal elements was carried out throughout the thickness of virgin and active devices (see Section S3, Supporting Information).

The bipolar switching behavior of STO-based MIM devices is largely attributed[16] to the nanoionics transport mechanisms and reversible redox reactions along the oxygen vacancy induced defect structure in TiO_2 sublattice.[2,10,31,32] Ti^{3+} species are the signature of charge transfer from oxygen vacancies to neighboring Ti atoms,[40,41] and therefore, the nanoionics transport processes largely take place along the Ti^{3+} suboxide network.[2,15,42,43] The relative concentration of as-grown Ti^{3+} species in the oxygen-deficient a-STO cells is 45%–65% higher than that of stoichiometric cells. a-STO oxides sputtered in pure argon atmosphere develop inherent oxygen vacancies due to heavy Ar^+ ion bombardment and preferential removal of oxygen atoms in the vacuum system.[43,44] Moreover, the

presence of oxygen during the sputtering of stoichiometric a-STO oxides facilitates negative ion creation and re-sputtering processes[44,45] that lead to the creation of misfit Ti^{2+} metallic suboxide species.[40,46] These stationary misfit species contribute to a greater degradation of the oxide layer during the high-field-forming process.

Nb3d spectrum of the Nb-doped oxygen-deficient a-STO devices consists solely of Nb^{5+} (Nb3$d_{5/2}$ peak at 206.86 eV)[47,48] species with a Nb/Ti ratio of 0.023, throughout the thickness of the oxide, where Nb^{5+} species substitutes Ti^{4+} site in the a-STO structure.[19,46] As the ionic radius of Nb^{5+} (0.069 nm) is very close to that of Ti^{4+} (0.068 nm), substitutional doping at such low concentrations is not expected to induce a transition in the electronic structure of the oxide.[19] However, the mismatch in the ionization of B-site species is likely to introduce additional bands and contribute to an overall reduction of the

bandgap. These additional electronic energy states provide an assistive role to the multistate bipolar switching behavior through nonlinear electron trapping/de-trapping and hopping mechanisms.[3,32]

Photoluminescence (PL) spectra of pristine and Nb-doped oxygen-deficient *a*-STO cells indicate a shift of the main energy states toward lower energies and the introduction of additional energy states as a result of niobium doping (see Section S4, Supporting Information). Hence, the dynamic evolution of the resistance of the Nb-doped MIM cells can be described by a time-evolving state function, which relies on the variability of the carrier hopping through multiple energy states[32] and creates a nonlinear drift of electronic and ionic carriers through the conducting channel.[32,49] This can further clarify the origin of non-Arrhenius behavior of HRS conductivity and the existence of multiple stable high-resistance states in Nb-doped MIM cells described earlier in the manuscript.

3.1. Evolution of Oxygen Vacancies and Ti Suboxides in *a*-STO Memristive Cells

In a typical electroforming step, the defect structure is extended from a *pseudo*-Ohmic electroforming cathode (grounded electrode) towards the blocking anode (positively biased inert electrode) via the migration of positively charged oxygen vacancies along the pre-existing defect structure. This results in the formation of a virtual cathode that can be extended (during SET) or abridged (during RESET) depending on the polarity of electrical field.[2] **Figure 3** depicts the XPS analysis of the evolution of oxygen deficiencies and Ti suboxide network carried out through the thickness of active oxygen-deficient *a*-STO memristive cells. Due to preferential removal of oxygen atoms and subsequent oxide reduction during the depth profile argon milling process, these results should be analyzed on the basis of comparative differences between Ti suboxides and oxygen concentrations in virgin and electroformed cells (see Figure S8, Supporting Information, for Ti spectra in virgin *a*-STO cells). O1*s* spectra averaged over the whole area at the interfacial region of *a*-STO MIM cells (Figure 3c) indicate a sharp decrease of oxygen content in the *a*-STO at the interfacial region. The oxygen concentration increases to almost the same level as in the virgin oxide (≈57%), beyond 30 nm from the interface. The large oxygen vacancy gradient in *a*-STO switching cells indicates the formation of virtual cathode regions at the top Ti/*a*-STO interface during the electroforming step. Together with large systematic variations in oxygen concentrations over the whole switching cell area, this indicates the existence of conduction and switching pathways over a large volume of the oxide similar to those reported in STO single crystals and acceptor-doped STO thin films.[14,26] As such, it appears that the electroforming and subsequent bipolar switching takes place across the entire *a*-STO MIM cell area. The evolution of Ti2*p* binding energy spectra in active *a*-STO MIM cells near the interfacial region (Figure 3d–f) complement the evidence for large volume redox-based switching process in *a*-STO memristive cells. In our previous report, we highlighted the existence of multifilamentary switching networks in *a*-STO oxides, which facilitate area-independent switching behavior over a large cell

volume.[16] In the following sections, we details the dynamics of multifilamentary switching behavior in *a*-STO oxides.

At the top Ti/*a*-STO interface, Ti2*p* spectra of active *a*-STO cells indicate the presence of a mixed metallic Ti/Ti$^{(2-\delta)+}$ phase with a reference Ti2*p*$_{3/2}$ binding energy of 453.5 eV. The peaks for Ti^{3+} and Ti^{4+} species appear at the same binding energies as in the virgin oxide, albeit with the relative Ti^{3+}/Ti^{4+} concentration dropping to 46% (from 65% for the virgin oxide). The appearance of a strong mixed phase is likely due to the presence of Ti layer residue at the top interface and oxidation of the Ti layer through oxygen exchange reactions during the forming process.

Further from the interface, the relative Ti^{3+}/Ti^{4+} concentration is around the same level as the virgin oxide (65%). Moreover, the Ti2*p*$_{3/2}$ peaks shift towards higher energy states (453.8 and 454.4 eV at 15 nm and 30 nm away from the interface, respectively) which signals the formation and extension of partially oxidized Ti$^{(2-\delta)+}$ phases in active MIM cells. Beyond 30 nm from the interface, the peak disappears and the configuration of Ti2*p* spectra is similar to that of the virgin devices. As such, the appearance of a metallic Ti suboxide network as a result of the electroforming step indicates the creation of conductive pathways, which extend from the top interface through the thickness of *a*-STO cells. This charge exchange along the Ti^{3+} network and the partial, reversible reduction of these species to a metallic phase accounts for the nonvolatile bipolar switching behavior observed in *a*-STO MIM cells.

4. *a*-STO Nanoswitches as Ultrafast Ion Transport Routes

In our previous study,[16] we demonstrated the distributed multifilamentary network of conductive channels in *a*-STO oxides (i.e., isolated nanoswitches), through load-controlled nanocontact studies (see Section S5, Supporting Information).[16,50,51] Here, to further ascertain the dynamics of the isolated resistive switching of nanoswitches in *a*-STO MIM cells, ultra low-load in situ electrical nanoindentation measurements were carried out. Nanocontacts with an estimated diameter of ≈35–40 nm were held constant on the top interface of an active *a*-STO cell in the ON state for a fixed time period (10 s) during the ultra low-load (25 μN peak load) in situ electrical nanoindentation experiments. The contact load was chosen to ensure that no mechanical deformations occur at peak load, in either the virgin cells or the nanoswitches. During the hold period at the peak mechanical load, cyclic switching step voltages were applied, while monitoring the current response and nanocontact displacements. This setup was used to accurately map the current transport of 2 μm × 2 μm *a*-STO cell regions through a large number (40 × 40 point arrays) of successive ultra low-load experiments. While the nondeformed areas in electroformed *a*-STO cells preserved their insulating properties, the nanoswitches exhibited a repeatable bipolar switching behavior (**Figure 4**a). These experiments were carried out for *a*-STO oxides with different compositions where no representative difference with regards to the distribution, structure, and transport properties of nanoswitches between different oxides was observed. This is in line with the observation of similar activation energies for
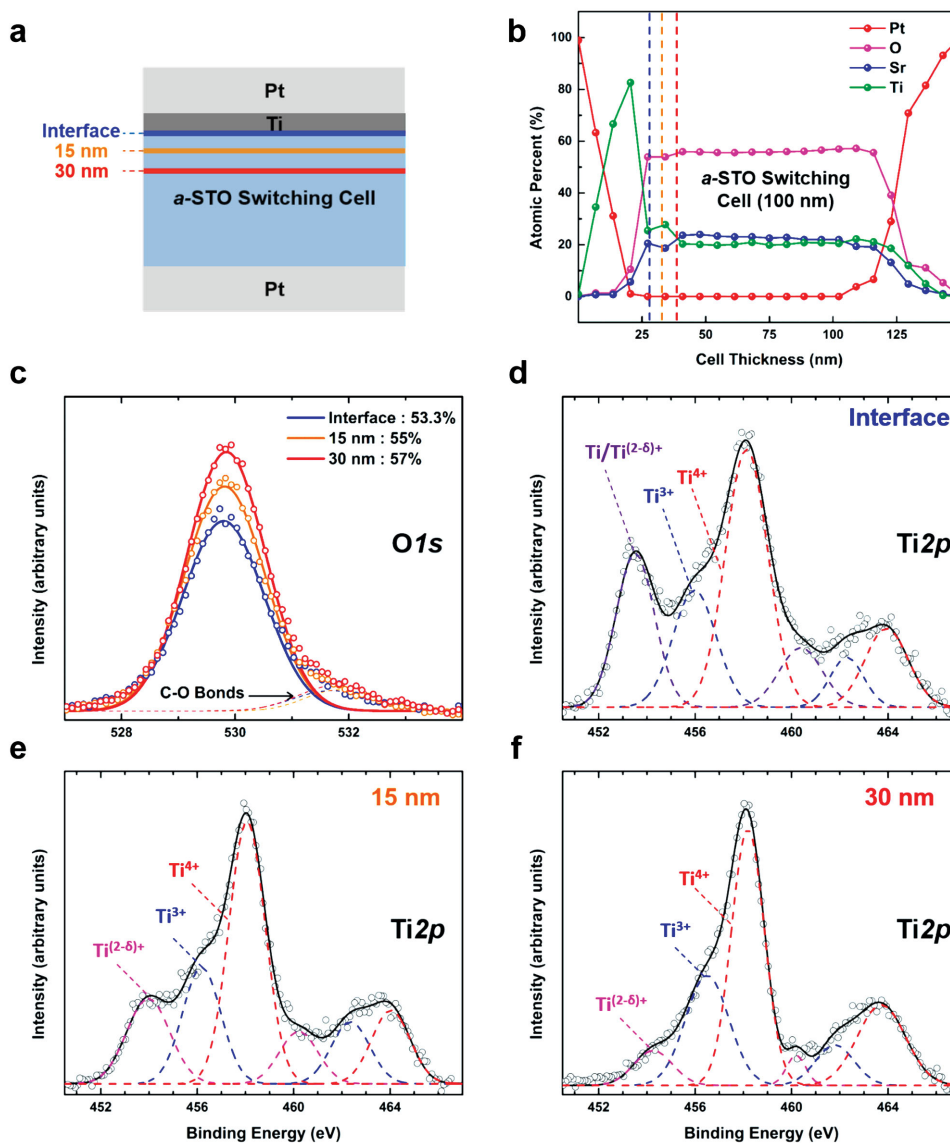
Figure 3. De-convolution of binding energy spectra of TiO$_2$ sublattice components throughout the thickness of *a*-STO cells. a) Schematic of an *a*-STO switching cell highlighting the relative depths of the analyzed spectra. b) Atomic concentrations of principle elements through the thickness of an active 100 μm²*a*-STO cell (dotted lines indicate different depths shown in schematic). c) O1s spectra of an active *a*-STO cell at different depths (corresponding to the horizontal lines in the schematic) relative to the top Ti/a-STO interface. d–f) Ti2p spectrum of the active *a*-STO cell at the same relative depths.

different oxides in LRS regime and indicates that the origins of variations in conductivity and memristive performance of the different oxides lie in different degrees of degradation, distribution of misfit phases, and trap sites, and electronic band structures of oxides with different defect chemistries. Nonetheless, a close examination of the time-correlated evolution of current transport upon applying SET and RESET voltages at the constant peak load provides further insights into the dynamical evolution of current transport in the nanoswitches.

Upon applying a step RESET voltage (300 mV) on the platinum electrode, the current flow through the grounded top nanocontact (Figure 4b) strongly resembles a capacitive discharge current where dI/dt < 0 with a calculated τ_c = 0.21 s. In considering the capacitive decay time constant for nanoswitches, the resistance imposed by nanocontact at 25 μN peak load has to be taken into account. At such low contact forces, the nanocontact resistance is in the range of 0.15–0.25 MΩ, depending on the surface roughness and average grain size of the sample.[16] As such, assuming a low-resistance Ohmic top contact, as is the case for *a*-STO MIM cells, would result in significantly reduced estimated time constants for nanoswitches according to $\tau_c = RC$.

On applying a step SET voltage (−300 mV) to a nanoswitch in OFF state from the platinum bottom electrode, the memristive mechanisms (the motion of oxygen vacancies towards the residual barrier at *a*-STO/Pt interface) become activated and the nanoswitch switches back to ON state. The memristive regime is exemplified by a positive and decaying current derivative (dI/dt ≥ 0). We further applied the memristive-based Cottrell equation proposed by Messerschmitt et al.[25] to derive

www.MaterialsViews.com

ADVANCED
FUNCTIONAL
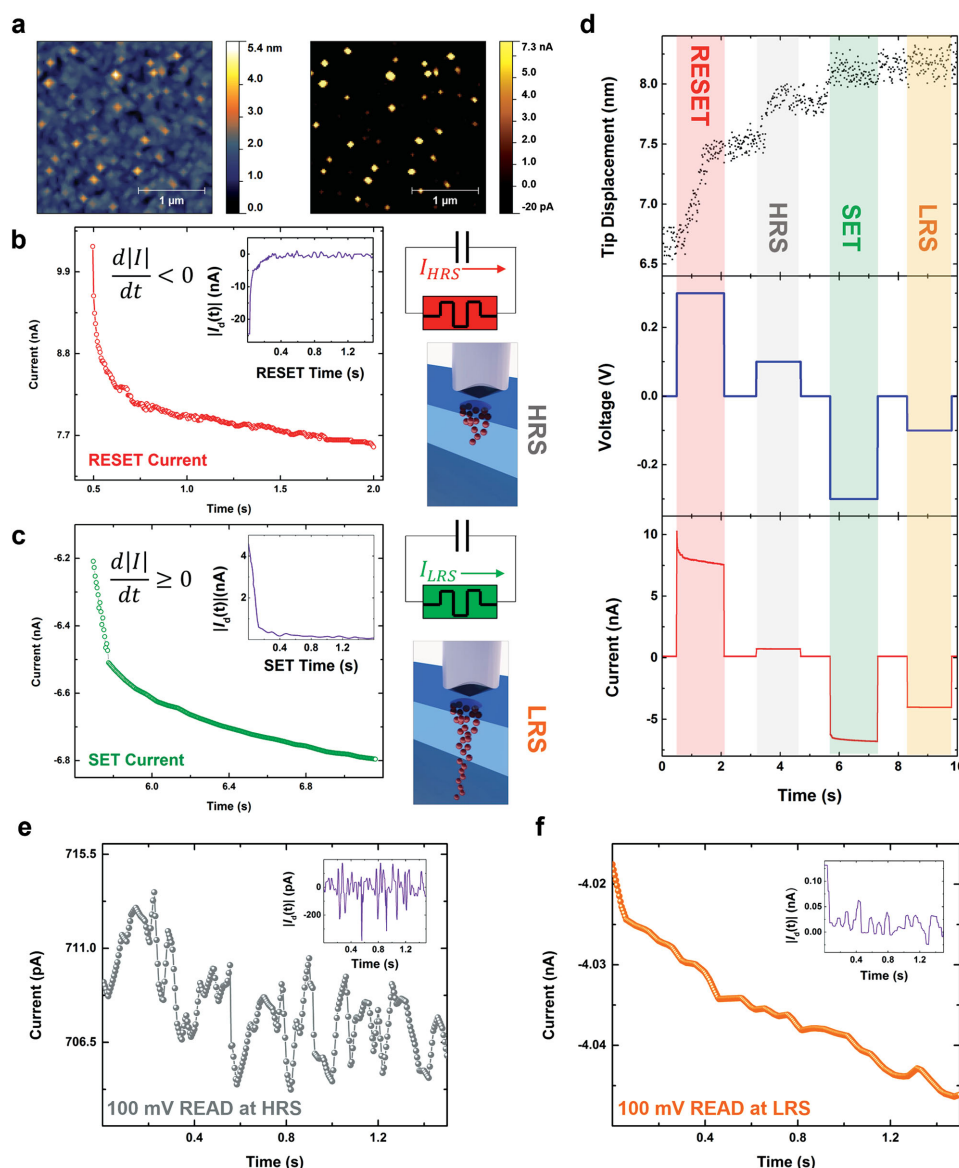MATERIALS
www.afm-journal.de

FULL PAPER

Figure 4. a) In situ SPM image of the surface (left) and compiled area conductivity map for nanocontact probing experiments (right) of a switching Nb-doped *a*-STO cell after removing the top metal electrode layers exhibiting distributed nanoswitches and their conductivity profile compared to the nondeformed regions. b,c) Time-based current evolution of a single nanoswitch upon applying SET/RESET step voltages (±300 mV) at 25 µN nanocontact load. The insets show the current derivatives in for each case. The schematics show the resistive states and current directions. d) Cyclic resistive switching of a single nanoswitch the time-based correlation of nanocontact displacements. Time-based current evolution of a single nanoswitch in e) HRS and f) LRS upon applying a high READ step voltage (±100 mV) with the same polarity as in SET/RESET step at 25 µN nanocontact load. The insets show the current derivatives in for each case (solid connector lines are added between the data points for clarity).

an estimate for the diffusion coefficient of oxygen vacancies in isolated nanoswitches. As the nanocontact cannot be held on top of the nanoswitch for an extended period of time due to thermal drift and surface friction effects, the transient memristive current data obtained for a period of 1.5 s, was extrapolated over time using a coupled exponential decay function the reach to a self-limiting current where $dI/dt < 10^{-11}$, indicating a steady state. The role of the series nanocontact resistance (≈200 kΩ ± 10%) has been eliminated by substituting an area-corrected resistance proportional to the overall resistance of a full MIM cell in the ON state.[16,50] Assuming a diffusion length

of 100 nm (the thickness of the oxide) for the nanoswitch, a diffusion constant of 5.27×10^{-15} m^2 s^{-1} was calculated for the nanoswitches. The anomalously high calculated diffusion constant likely originates from an overestimation of the diffusion length; i.e., the migration length of oxygen vacancies along the nanoswitches for a switching transition is likely to be only a small fraction of the oxide length. Nonetheless, this demonstrates that extremely localized charge transport along the extended defect structure of nanoswitches facilitates higher directional mobilities for the diffusive oxygen vacancy species. This is also supported by current response of the nanoswitches

in LRS and HRS regimes subject to high READ voltages (±100 mV: 33% of the RESET/SET voltages) where the current derivatives are in sub-nanoampere regime.

The abrupt changes in the current transport regimes can also be correlated with unique bursts in the time versus displacement data observed upon switching the voltage to ±300 mV (ERASE/WRITE) values (Figure 4d). As evident, the structure of the grains is not altered by such low-load nanocontacts (i.e., the grains are not deformed or flattened). These observed displacement bursts appear to be due to the instantaneous shift of charged species upon switching, which drastically changes the charge equilibrium and adhesion forces at the contact area; thereby, displacing the contact.[52,53] These results further confirm that the memristive behavior of a-STO cells and nanoswitches originates from the movement of oxygen vacancy species along the extended defect structures.

5. Nb-Doped a-STO Nanoislands

We further explored the scalability of memristive performance of Nb-doped a-STO devices via force-controlled nanocontact experiments using 10 nm (±0.3 nm) thick and 300 nm in diameter nanoislands defined by electron beam lithography (EBL) on to Pt-coated substrates, as depicted in **Figure 5**a (see Experimental Details section for fabrication parameters). We avoided using the Pt/Ti top metal electrodes in this case and instead used the conductive ceramic tip (with a high metal work function of ≈5.1 eV) as a top contact to enable a direct study of redox processes in the oxide layer. Nanocontacts with 25 and 50 μN loads (corresponding to 18.2 and 24.3 nm contact diameters, as shown in Figure 5b) were employed to investigate their memristive performance. As depicted in Figure 5b, the mechanical response of nanoislands is mainly elastic under such contact loads. All in situ electrical measurements results were corrected to isolate and remove the effect of decreasing nanocontact resistance with increasing force using the empirical method reported previously.[50]

Initially, the as-synthesized nanoislands exhibited an insulating behavior with a Schottky-like transport characteristic arising due to surface oxidation. Voltage sweeps with a peak voltage of 1 V were used as forming voltages for Nb-doped a-STO nanoislands with a 100 nA current compliance limit to avoid extensive morphological breakdowns (Figure 5c).[16] No detectable mechanical deformation was observed in the island structure after the electroforming step with peak contact loads of 50 μN, which indicates that the slight residual contact depth at this load originates from the associated thermal drift and friction/electrostatic effects during the electrical measurements. Subject to increasing nanocontact loads, the required forming voltage drops. This can be ascribed to an increased concentration of dislocation sites, which results in the modulation of out-of-plane oxygen diffusion in the amorphous lattice.[16,21] Following the electroforming step, the nanoislands exhibit a reproducible bipolar switching behavior (Figure 5d). Interestingly, the LRS currents in both polarities and subsequently the switching ratios increase by almost 40% as the nanocontact force is increased from 25 to 50 μN (corresponding to a 3.1 GPa increase in the mechanical pressure), after correcting

for the increase in the nanocontact area. This points to a force-induced modulation of dislocation sites and ionic transport along the extended defects formed upon electroforming and is further backed by in situ constant bias experiments on nanoislands in the HRS and LRS regimes (Figure 5e). In the HRS regime, the nanocontact currents remain below the measurement noise level during the loading and unloading segments under 10 mV bias. This indicates that, while the mechanical force is likely to modulate the electronic charge distribution and mobility and, consequently the capacitive discharge in Nb-doped a-STO nanoislands in HRS regime, the leakage current along the recovered electronic does not surpass the measurement sensitivity. On the other hand, in the LRS regime, a clear upward trend is observed with increasing mechanical pressure, which cannot be adequately justified by the increase in nanocontact area. The origin of the force-modulated conduction in the LRS regime is perceived to be majorly relying on the modulated mobility of oxygen vacancies through the conudctive pathways, which can translate to a force-dependent current across the metal–oxide interface.

6. Conclusion

We have investigated the dynamics and temperature dependence of the memristive performance of a-STO-based devices with an emphasis on the role of as-grown oxygen vacancy network and donor-induced dislocation sites. Particularly, we have demonstrated that the donor doping in a-STO network, improves the stability and controllability of the memristive performance. Donor doping allows for multistate switching through increasing the electronic current contribution and the introduction of dislocation sites and additional energy states in the oxide band structure. We have also showcased the ultimate scalability of donor-doped devices by investigating the switching performance of Nb-doped a-STO nanoislands utilizing a force-controlled nanocontact technique. Overall, these results showcase the immense potential of Nb-doped a-STO oxides for high-density integration in memory and logic systems. Moreover, the mechanical modulation of current transport opens doors for the design and fabrication of multifunctional devices and systems.

7. Experimental Section

Oxygen-Deficient a-STO Thin Films without and with Nb-Doping: 100 nm a-STO thin films with different compositions were deposited on Pt/TiO$_2$/SiO$_2$ (50:10:300 nm)-coated Si substrates using RF magnetron sputtering at room temperature, from a stoichiometric ceramic target. Oxygen-deficient a-STO thin films were realised through sputtering in a pure argon atmosphere. Nb dopant species were incorporated into a-STO thin films via co-sputtering utilizing ceramic STO and metallic Niobium targets. Thin films were sputtered with a sputtering pressure of 5 mTorr (from a base pressure <10^{-7} Torr). Detailed sputtering conditions are presented in Section S1(Supporting Information).

a-STO Crossbar Devices: Microscale a-STO crossbar arrays were fabricated on SiO$_2$/Si substrates using a three-step photolithography/lift-off process. In the first lift-off step, 50 nm bottom platinum electrodes

www.MaterialsViews.com

ADVANCED
FUNCTIONAL
MATERIALS
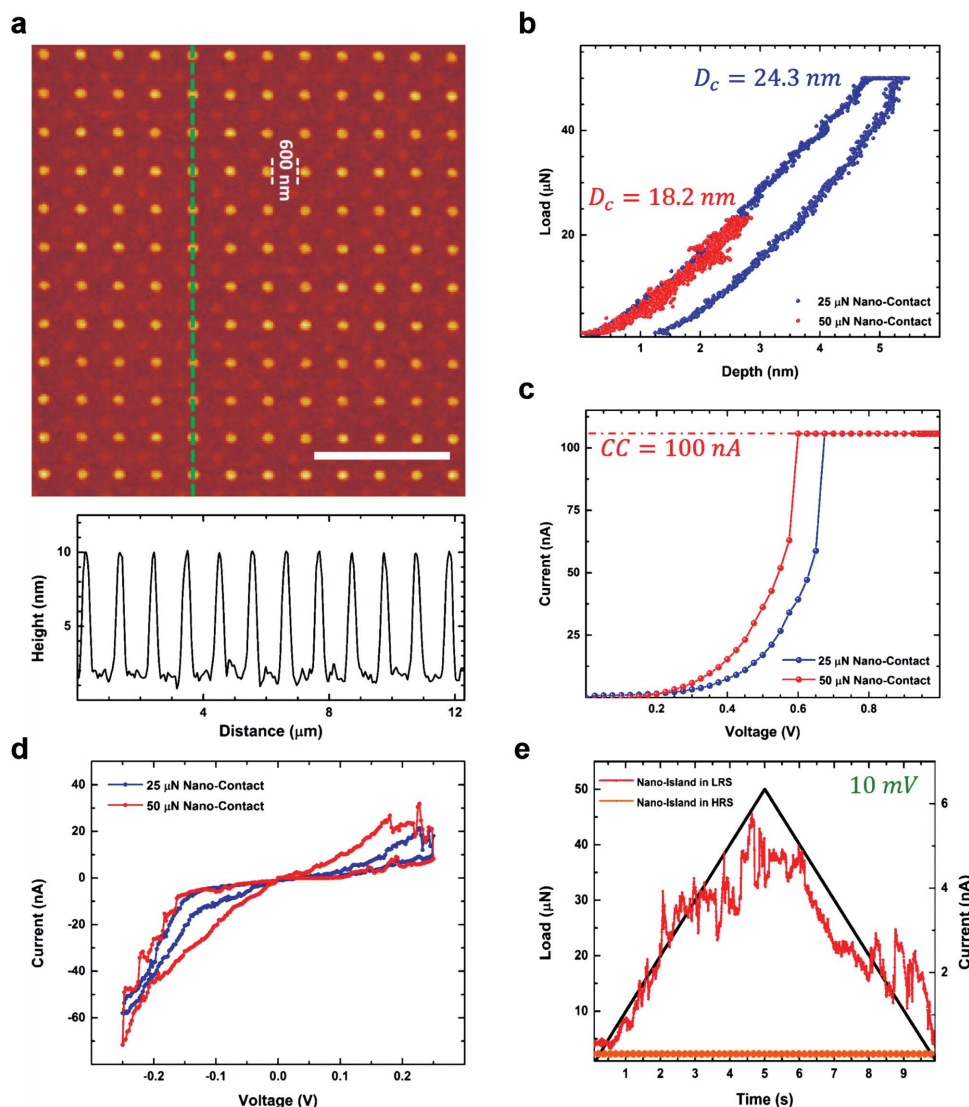www.afm-journal.de

FULL PAPER

Figure 5. Force-controlled nanocontact experiment on Nb-doped *a*-STO nanoislands. a) Scanning probe microscopy scan of an array of nanoislands (10 ± 0.4 nm thick with a 300 nm diameter, scale bar: 4 µm). b,c) Load–displacement and I–V responses of 25 and 50 µN nanocontact experiments on the nanoislands. Voltage sweeps were performed at the constant peak load. d) Bipolar I–V behavior of formed nanocontacts under 25 and 50 µN loads. e) Current response of nanoislands in HRS and LRS subject to increasing nanocontact force under 10 mV bias.

with 10 nm TiO$_2$ adhesion layers were deposited on pre-patterned SiO$_2$/Si substrates by electron beam evaporation at room temperature. *a*-STO thin films of 100 nm thickness were then RF sputtered through a shadow mask. Lastly, Pt/Ti (50:10 nm) top electrodes were deposited by electron beam evaporation at room temperature and patterned using photolithography to complete the crossbar structure.

Nb-Doped a-STO Nanoislands: A 250-nm-thick polymethylmethacrylate (PMMA) layer was applied to the Pt/TiO$_2$/SiO$_2$/Si substrates via spin coating followed by a hard bake at 180 °C. PMMA was then exposed with an EBM system (Nabity EBL system on a FEI Nova SEM equipped with a field emission gun) writing the negative mask of the nanoislands in a serial process. Nb-doped *a*-STO thin films were deposited on patterned substrates via co-sputtering with the same conditions as the thin films. The samples were then lifted off in acetone to realize the nanoislands structures.

Electrical Characterization of Cross-bar Devices: The electrical characterization of *a*-STO crossbar devices was performed using an Agilent 2912A sourcemeter for two-probe and four-probe direct current

and pulse transient measurements assigning the top electrode of MIM cells as the ground electrode.

X-Ray Photoelectron Spectroscopy: XPS surface and depth profile analyses were carried out using a Thermo Scientific K-Alpha instrument. An aluminum Kα radiation source with energy of 1485 eV was used, with the adventitious carbon peak (at 284.8 eV) used as the calibration reference for fitting of the core level spectra of the principal elements. The composition of the films was determined utilizing the area under the curves, fitted, and corrected with sensitivity factors using the Avantage data system. Depth profiling was performed by successive, cyclic argon-ion etch, and spectral acquisition processes.

In Situ Electrical Nanoindentation: Nanoindentation experiments with in situ electrical measurements were carried out using Hysitron's NanoECR system on a TI 950 Triboindenter. A conductive Pulsar Berkovich tip was used, with the nanoindentation technique enabling the in situ measurement of electrical contact resistance between the indenter tip and the specimen. Details of the experimental setup and measurement procedures can be found in our previous reports.[16,51,54]

FULL PAPER

Supporting Information

Acknowledgements

[1] A. Sawa, *Mater. Today* **2008**, *11*, 28.

[2] R. Waser, R. Dittmann, G. Staikov, K. Szot, *Adv. Mater.* **2009**, *21*, 2632.

[3] J. Yang, D. Strukov, D. Stewart, *Nat. Nanotechnol.* **2013**, *8*, 13.

[4] J. J. Yang, M. D. Pickett, X. Li, D. A. Ohlberg, D. R. Stewart, R. S. Williams, *Nat. Nanotechnol.* **2008**, *3*, 429.

[5] J. Shang, G. Liu, H. Yang, X. Zhu, X. Chen, H. Tan, B. Hu, L. Pan, W. Xue, R. W. Li, *Adv. Funct. Mater.* **2014**, *24*, 2171.

[6] D. B. Strukov, H. Kohlstedt, *MRS Bull.* **2012**, *37*, 108.

[7] X. Guo, J. Fleig, J. Maier, *J. Electrochem. Soc.* **2001**, *148*, J50.

[8] R. Hagenbeck, R. Waser, *J. Appl. Phys.* **1998**, *83*, 2083.

[9] K. Szot, W. Speier, G. Bihlmayer, R. Waser, *Nat. Mater.* **2006**, *5*, 312.

[10] R. Muenstermann, T. Menke, R. Dittmann, R. Waser, *Adv. Mater.* **2010**, *22*, 4819.

[11] T. Menke, R. Dittmann, P. Meuffels, K. Szot, R. Waser, *J. Appl. Phys.* **2009**, *106*, 114507.

[12] K. Szot, R. Dittmann, W. Speier, R. Waser, *Phys. Status Solidi (RRL) – Rapid Res. Lett.* **2007**, *1*, R86.

[13] C. Lenser, Z. Connell, A. Kovács, R. Dunin-Borkowski, A. Köhl, R. Waser, R. Dittmann, *Appl. Phys. Lett.* **2013**, *102*, 183504.

[14] R. Muenstermann, R. Dittmann, K. Szot, S. Mi, C.-L. Jia, P. Meuffels, R. Waser, *Appl. Phys. Lett.* **2008**, *93*, 023110.

[15] R. Waser, M. Aono, *Nat. Mater.* **2007**, *6*, 833.

[16] H. Nili, S. Walia, S. Balendhran, D. B. Strukov, M. Bhaskaran, S. Sriram, *Adv. Funct. Mater.* **2014**, 6741.

[17] C. Rodenbücher, W. Speier, G. Bihlmayer, U. Breuer, R. Waser, K. Szot, *New J. Phys.* **2013**, *15*, 103017.

[18] S. Dai, H. Lu, F. Chen, Z. Chen, Z. Y. Ren, D. H. L. Ng, *Appl. Phys. Lett.* **2002**, *80*, 3545.

[19] S. Shibagaki, K. Fukushima, *J. Eur. Ceram. Soc.* **1999**, *19*, 1423.

[20] T. D. Nguyen, S. Mao, Y.-W. Yeh, P. K. Purohit, M. C. McAlpine, *Adv. Mater.* **2013**, *25*, 946.

[21] R. Al-Hamadany, J. Goss, P. Briddon, S. A. Mojarad, A. G. O'Neill, M. J. Rayson, *J. Appl. Phys.* **2013**, *113*, 224108.

[22] J. H. Haeni, P. Irvin, W. Chang, R. Uecker, P. Reiche, Y. L. Li, S. Choudhury, W. Tian, M. E. Hawley, B. Craigo, A. K. Tagantsev, X. Q. Pan, S. K. Streiffer, L. Q. Chen, S. W. Kirchoefer, J. Levy, D. G. Schlom, *Nature* **2004**, *430*, 758.

[23] P. Zubko, G. Catalan, A. Buckley, P. R. L. Welche, J. F. Scott, *Phys. Rev. Lett.* **2007**, *99*, 167601.

[24] D. Kan, T. Terashima, R. Kanda, A. Masuno, K. Tanaka, S. Chu, H. Kan, A. Ishizumi, Y. Kanemitsu, Y. Shimakawa, *Nat. Mater.* **2005**, *4*, 816.

[25] F. Messerschmitt, M. Kubicek, S. Schweiger, J. L. Rupp, *Adv. Funct. Mater.* **2014**, *24*, 7448.

[26] S. Stille, C. Lenser, R. Dittmann, A. Koehl, I. Krug, R. Muenstermann, J. Perlich, C. M. Schneider, U. Klemradt, R. Waser, *Appl. Phys. Lett.* **2012**, *100*, 223503.

[27] I. Denk, J. Claus, J. Maier, *J. Electrochem. Soc.* **1997**, *144*, 3526.

[28] U. Balachandran, N. Eror, *J. Solid State Chem.* **1981**, *39*, 351.

[29] R. A. De Souza, J. Fleig, J. Maier, Z. Zhang, W. Sigle, M. Rühle, *J. Appl. Phys.* **2005**, *97*, 053502.

[30] K. Shibuya, R. Dittmann, S. Mi, R. Waser, *Adv. Mater.* **2010**, *22*, 411.

[31] R. Dittmann, R. Muenstermann, I. Krug, D. Park, T. Menke, J. Mayer, A. Besmehn, F. Kronast, C. M. Schneider, R. Waser, *Proc. IEEE* **2012**, *100*, 1979.

[32] D. B. Strukov, J. L. Borghetti, R. S. Williams, *Small* **2009**, *5*, 1058.

[33] R. Meyer, R. Liedtke, R. Waser, *Appl. Phys. Lett.* **2005**, *86*, 112904.

[34] F. Horikiri, N. Iizawa, L. Han, K. Sato, K. Yashiro, T. Kawada, J. Mizusaki, *Solid State Ionics* **2008**, *179*, 2335.

[35] R. A. De Souza, *Phys. Chem. Chem. Phys.* **2009**, *11*, 9939.

[36] G. Herranz, M. Basletić, O. Copie, M. Bibes, A. N. Khodan, C. Carrétéro, E. Tafra, E. Jacquet, K. Bouzehouane, A. Hamzić, A. Barthélémy, *Appl. Phys. Lett.* **2009**, *94*, 012113.

[37] F. Horikiri, L. Q. Han, A. Kaimai, T. Otake, K. Yashiro, T. Kawada, J. Mizusaki, *Solid State Ionics* **2006**, *177*, 2555.

[38] C. Lenser, A. Kuzmin, J. Purans, A. Kalinko, R. Waser, R. Dittmann, *J. Appl. Phys.* **2012**, *111*, 076101.

[39] F. Alibart, E. Zamanidoost, D. B. Strukov, *Nat. Commun.* **2013**, *4*, 2072.

[40] J. Brunen, J. Zegenhagen, *Surf. Sci.* **1997**, *389*, 349.

[41] K. Morii, H. Kawano, I. Fujii, T. Matsui, Y. Nakayama, *J. Appl. Phys.* **1995**, *78*, 1914.

[42] R. Merkle, J. Maier, *Angew. Chem. Int. Ed.* **2008**, *47*, 3874.

[43] K. B. Lee, K. H. Lee, J. O. Cha, J. S. Ahn, *J. Korean Phys. Soc.* **2008**, *53*, 1996.

[44] H. Nili, A. E. Kandjani, J. Du Plessis, V. Bansal, K. Kalantar-zadeh, S. Sriram, M. Bhaskaran, *CrystEngComm* **2013**, *15*, 7222.

[45] Z. Wang, V. Kugler, U. Helmersson, E. Evangelou, N. Konofaos, S. Nakao, P. Jin, *Phil. Mag. B* **2002**, *82*, 891.

[46] B. C. Russell, M. R. Castell, *Phys. Rev. B* **2008**, *77*, 245414.

[47] S. Kundu, Y. Wang, W. Xia, M. Muhler, *J. Phys. Chem. C* **2008**, *112*, 16869.

[48] K. Jung, Y. Kim, Y. S. Park, W. Jung, J. Choi, B. Park, H. Kim, W. Kim, J. Hong, H. Im, *J. Appl. Phys.* **2011**, *109*, 054511.

[49] D. Strukov, R. S. Williams, *Appl. Phys. A* **2009**, *94*, 5151.

[50] H. Nili, S. Walia, M. Bhaskaran, S. Sriram, *J. Appl. Phys.* **2014**, *116*, 163504.

[51] H. Nili, G. Cheng, T. Venkatesh, S. Sriram, M. Bhaskaran, *Mater. Lett.* **2013**, *90*, 148.

[52] J. X. Zhang, B. Xiang, Q. He, J. Seidel, R. J. Zeches, P. Yu, S. Y. Yang, C. H. Wang, Y. H. Chu, L. W. Martin, A. M. Minor, R. Ramesh, *Nat. Nanotechnol.* **2011**, *6*, 98.

[53] R. Nowak, D. Chrobak, S. Nagao, D. Vodnick, M. Berg, A. Tukiainen, M. Pessa, *Nat. Nanotechnol.* **2009**, *4*, 287.

[54] H. Nili, K. Kalantar-Zadeh, M. Bhaskaran, S. Sriram, *Prog. Mater. Sci.* **2013**, *58*, 1.